Earth and Planetary Science Letters 587 (2022) 117537

Contents lists available at ScienceDirect

Earth and Planetary Science Letters

www.elsevier.com/locate/epsl

Core segregation during pebble accretion

Peter Olson *, Zachary Sharp, Susmita Garai

Earth and Planetary Sciences, University of New Mexico, United States of America

ARTICLE INFO

Article history:
Received 27 December 2021
Received in revised form 30 March 2022
Accepted 8 April 2022
Available online xxxx
Editor: J. Badro

Keywords:
pebble accretion
core segregation
nebular atmosphere
magma ocean
metal-silicate equilibration

ABSTRACT

We present a model for terrestrial planet formation by pebble accretion, focusing on core segregation in the early Earth. Our results indicate that if the proto-Earth and the Moon-forming impactor Theia grew by pebble accretion, core-forming metals in each body segregated from mantle-forming silicates within the first few million years of solar system history, while both were enveloped in atmospheres composed of nebular gas. Thermal blanketing by their energy-absorbing atmospheres, heat produced by radioactive decay of aluminum-26, and gravitational energy released by metal segregation resulted in very high internal temperatures, such that the mantle and core of both bodies experienced partial or total melting during accretion. We calculate pressure-temperature conditions where the core-forming metals are predicted to have segregated from magma ocean silicates under pebble accretion. Two-body combinations of these conditions, representing the merger of proto-Earth and Theia, yield average segregation pressures and temperatures that are similar to core segregation conditions previously inferred for impact-driven Earth accretion constrained by metal-silicate partitioning of siderophile elements.

1. Introduction

A central premise on which most current theories of core formation in terrestrial planets are based is that core-forming metals segregated from mantle-forming silicates during the planet accretion process (Rubie and Jacobson, 2016). In addition, isotopic evidence indicates that prior to segregation, the core-forming metals partially or fully equilibrated with silicate melt (Kleine and Walker, 2017), implying that the present-day mantle composition holds clues as to the physical conditions under which that segregation took place.

The most widely-considered theory of core segregation is that it took place in discrete steps, each segregation step a consequence of melting produced either by radioactive heating (Monteux et al., 2009) or by a large, energy-dissipating impact (Rubie et al., 2015; Kendall and Melosh, 2016). Upon melting, core-forming metals equilibrated with, and then segregated from, molten silicates within proto-Earth's mantle, near the base of a magma ocean and at a depth roughly corresponding to the intersection of the geotherm and the silicate liquidus (Wood et al., 2006).

Support for these events comes from several lines of evidence. Application of metal-silicate partitioning of siderophile elements to magma oceans has yielded geophysically consistent models of the present-day composition of the core (Badro et al., 2015; Fischer et al., 2017). In addition, laboratory fluid dynamics experiments and calculations (Wacheul and Le Bars, 2018; Clesi et al., 2020; Landeau et al., 2021) reveal that small and medium-sized impacting metal cores are expected to disperse and partially equilibrate with molten silicates on descent through a magma ocean. Theoretical considerations (Stevenson, 1990) and lab experiments (Fleck et al., 2018) indicate that if the magma ocean has a solid base, dispersed metals accumulate into large diapirs there, implying that little further equilibration occurs as these diapirs sink into the core.

Recently, however, a competing theory of planet formation has emerged, in which large impacts are not the primary accretion mechanism. Astronomical observations of protoplanetary disks (Pérez et al., 2015; Andrews, 2015; Carasco-González et al., 2019) have determined that a substantial portion of the solid material surrounding very young stars resides in millimeter-to-centimeter-sized condensates, collectively referred to as *pebbles*. The aggregate pebble mass orbiting some young stars has been estimated to exceed one hundred Earth masses (Powell et al., 2019), with total solids (dust, pebbles, and larger bodies) amounting to between one and ten percent of the mass of the surrounding nebular gas (Ansdell et al., 2016).

Other astronomical observations indicate that pebble and dust abundances decrease on a time scale of a few million years (Tychoniec et al., 2018), presumably due to radial drift toward the central star. The orbital velocity of the nebular gas is sub-Keplerian because it is subject to a radial pressure force. Solids orbiting within a protoplanetary disk therefore experience a headwind from the slower rotating gas; the aerodynamic drag from this headwind

* Corresponding author.
E-mail address: peterleeolson@unm.edu (P. Olson).

https://doi.org/10.1016/j.epsl.2022.117537
0012-821X/

decreases the pebble angular momentum, forcing them to drift radially inward. Inward drifting pebbles are then gravitationally captured by planetesimals (Eriksson et al., 2020) and by higher mass protoplanets (Voelkel et al., 2012), particularly those that have acquired extensive nebular atmospheres of their own (Popovas et al., 2018).

Calculations show that the rate of inward pebble drift and their settling rate (the rate of gravitational capture by a protoplanet) is high around young solar-mass stars (Johansen and Lambrechts, 2017), such that protoplanets can acquire Earth-like masses within the lifetime of the stellar nebula gas, that is, within a few million years. The accretion energy released by incoming pebbles is expected to heat the nebular atmosphere, leading to very high temperatures on the protoplanet surface, and in conjunction with heating by short-lived radioactive isotopes and gravitational energy released during segregation, still higher temperatures in its interior. Consequently, core segregation processes are predicted to have occurred under high temperature conditions in the proto-Earth during pebble accretion.

Quantitative models of pebble accretion were first applied to gas giant planet formation (Lambrechts and Johansen, 2012), because other mechanisms, such as random planetesimal accretion (Bottke et al., 2010), typically fail to grow a critical mass core[1] within the short nebula lifetime (Nimmo et al., 2018). Pebble accretion has now been extended to terrestrial planets (Levison et al., 2015; Morbidelli et al., 2015), with some success in rationalizing the masses, compositions, and water contents of Earth and Mars (Ida et al., 2019; Johansen et al., 2021) Other calculations show that spatially heterogeneous pebble accretion can, under some circumstances, produce rapid protoplanet rotation (Visser et al., 2020).

Here we apply a simplified one-dimensional, time dependent model of pebble accretion for terrestrial planet formation to metal-silicate segregation and core formation processes in the proto-Earth and its Moon-forming impactor Theia. Our model includes an idealized nebular atmosphere above an idealized accreting protoplanet, the protoplanet consisting of silicate and metal components derived from pebbles. We calculate the metal segregation temperature and pressure as a function of time and final protoplanet mass. Two-body combinations, simulating the merger of the proto-Earth and Theia, yield average segregation temperatures and pressures compatible with core formation conditions inferred from multi-stage impact-based models constrained by metal-silicate partitioning of siderophile elements.

2. Pebble accretion

The efficiency of pebble accretion depends critically on two dimensionless parameters: the Stokes number of the pebbles (sometimes called the dimensionless stopping time), the product of the timescale for deceleration of a pebble due to aerodynamic drag τ_d and the local Keplerian orbital angular velocity Ω:

$$St = \tau_d \Omega, \tag{1}$$

and the headwind number,

$$Z_{hw} = \frac{v_{hw}}{r_{Hill}\Omega}. \tag{2}$$

Here v_{hw} is the headwind velocity, the velocity of the protoplanet relative to pebbles on the same orbit, and r_{Hill} is the radius of the Hill sphere,

[1] For giant planets, the term *core* usually refers to all dense solids near the planet center; here it refers only to iron-nickel alloys.

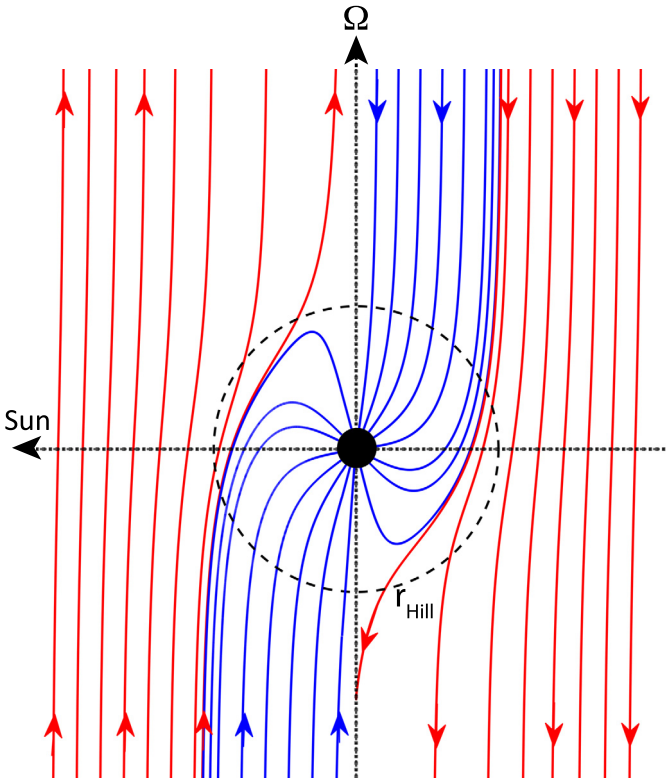

Fig. 1. Pebble trajectories in the orbital plane of a protoplanet, calculated for Stokes number St=0.1 and headwind number Z_{hw}=0.1, as described in the Appendix. Arrows indicate pebble motions relative to the protoplanet (dark circle; size exaggerated). Trajectories of pebbles that settle onto the protoplanet are shown in blue, escaping pebble trajectories in red. Orbital direction indicated by Ω; r_{Hill} denotes the radius of the Hill sphere. (For interpretation of the colors in the figures, the reader is referred to the web version of this article.)

$$r_{Hill} = (\frac{M}{3M_S})^{1/3}\mathcal{R}, \tag{3}$$

where M_S is the stellar mass and M and $\mathcal{R}$ are the mass and the orbital radius of the protoplanet.

An important criterion for pebbles to settle onto a protoplanet is that they be aerodynamically small, i.e., St cannot be too large (Johansen and Lambrechts, 2017). However, if the Stokes number is too small, say $St << 10^{-3}$, the capture cross-section for pebble settling diminishes and pebble accretion becomes less efficient (Ormel and Klahr, 2010). The most efficient regime for pebble accretion is the so-called Hill regime, where St lies in the range $10^{-3} - 10^{-1}$, roughly corresponding to millimeter-to-centimeter sizes. In the Hill regime, pebble settling occurs through a combination of headwind (pebble approach), crosswind (pebble drift toward the star), Keplerian shear (variations in pebble angular velocity with orbital distance), and gravitational attraction.

Fig. 1 shows pebble trajectories relative to an orbiting protoplanet in the Hill regime with $St = Z_{hw} = 0.1$, calculated using methods described in the Appendix. Arrows indicate the relative pebble motion directions, and colors distinguish settling versus escaping pebbles. With these parameters the pebble stopping time is approximately 6 days, the characteristic pebble diameter is a few centimeters, the headwind and crosswind are approximately 20 m/s and 4 m/s, respectively, and a terrestrial-size protoplanet on Earth's orbit captures 5-10% of inward drifting pebbles. Because of Keplerian shear, pebbles settle from inside as well as outside the protoplanet orbit, and the pebble capture cross-section is large for these parameters, approximately the diameter of the Hill sphere.

The protoplanet mass increases with time t according to

$$\frac{dM}{dt} = F, \tag{4}$$

where F is the pebble settling rate (mass flux). Provided the pebbles are concentrated within r_{Hill} of the orbital plane, two-dimensional accretion is valid. As demonstrated in the Appendix, the two-dimensional pebble settling rate with $St = Z_{hw} = 0.1$ is approximately

$$F = 2r_{Hill}^2 \Omega \Sigma, \tag{5}$$

where Σ is the column density of pebbles near the protoplanet orbit.

Access to pebbles is expected to have changed with time, and essentially vanished with the dissipation of the solar nebula. Accordingly, we adopt a time-dependence for the pebble column density at the proto-Earth orbit of the form

$$\Sigma = \Sigma_0 e^{-(t/\tau_n)^2}, \tag{6}$$

where Σ_0 is the initial column density and τ_n is the nebula dissipation timescale. Observations suggest a dissipation timescale $\tau_n \simeq 3$ Myr (Tychoniec et al., 2018), so that the pebble column density given by (6) becomes vanishingly small after ~6 Myr, consistent with the upper limit on chondrule ages (Villeneuve et al., 2009).

Because Jupiter and Saturn may have starved the terrestrial protoplanets of incoming pebbles (Morbidelli et al., 2015), we adopt relatively small initial pebble densities, Σ_0=0.2-0.3 kg/m^2. The pebble settling radius increases like $St^{2/3}$ in the Hill regime, so the quantity $\Sigma St^{2/3}$ is a measure of the abundance of captured pebbles. In our model, $\Sigma_0 St^{2/3}$=0.043-0.065 kg/m^2. For comparison, Johansen et al. (2021) assume fixed pebble size but larger initial pebble density, which combine to yield $\Sigma_0 St^{2/3} \simeq 0.1$ kg/m^2 for their terrestrial protoplanets. Unlike Johansen et al. (2021), we assume fixed orbits for proto-Earth and Theia, and consequently a fixed nebular temperature.

The pebble mass is divided into mantle-forming and core-forming components, referred to as "silicate" and "metal", respectively. We assume a constant proportionality between the masses of these two pebble types, with μ=0.32 for the metal fraction. Although this binary mixture does not reflect the actual compositions of the solids in the protoplanetary disk (which are better characterized as carbonaceous and noncarbonaceous), it is a convenient idealization for tracking core segregation processes. We further assume that pebble settling is independent of μ, so that the influxes of mantle-forming silicates and core-forming metals remain in constant proportion and the accreted metal and silicate masses are given by μM and $(1-\mu)M$, respectively.

We assign uniform densities to the silicate and metal components, denoted by ρ_m (the subscript m for mantle-forming) and ρ_c (the subscript c for core-forming), respectively. We ignore the effects of temperature, pressure, and redox reactions on these densities, in order to keep our results as transparent as possible. Because the densities of differentiated silicates and metals in the protoplanet are set equal to their respective component densities, the bulk density of the undifferentiated composite (denoted by subscript u) is related to the accreted protoplanet mass and the metal and silicate volumes by $\rho_u = M/(V_c + V_m)$, in which

$$V_c = \frac{\mu M}{\rho_c}; \qquad V_m = \frac{(1-\mu)M}{\rho_m}. \tag{7}$$

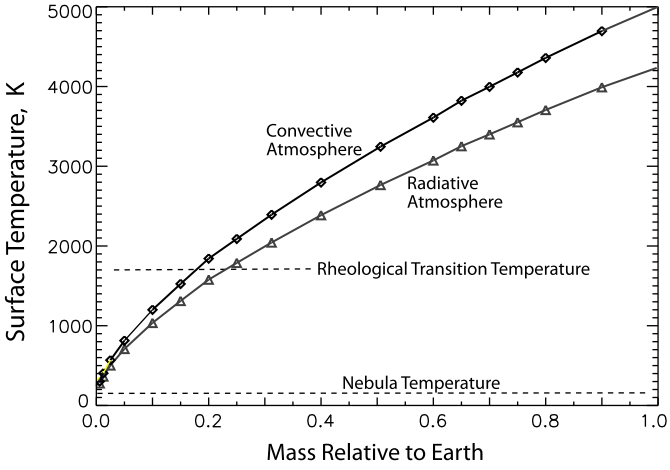

Fig. 2. Surface temperature versus protoplanet mass calculated for pebble accretion under uniform equilibrium radiative and convective nebular atmospheres. Dashed lines denote the model rheological transition temperature for surface magma ocean behavior and nebula temperature at proto-Earth's orbit, respectively.

3. Nebular atmosphere temperature

As the masses of the protoplanets increase, they gravitationally attract atmospheres composed of nebula gas. Previous investigations (Ikoma and Genda, 2006) have shown that nebular atmospheres develop a two-layer or three-layer structure, consisting of an outermost nearly isothermal layer, inside of which there are one or two layers with either radiative or convective temperature profiles. For our purposes it is sufficient to model only the lower part of the inner layer of the atmosphere, the region in direct contact with the protoplanet surface.

With uniform luminosity and opacity, the equilibrium atmosphere temperature varies inversely with radial distance from the protoplanet center r according to (see Appendix)

$$T = \frac{GM}{\gamma r} + T_n, \tag{8}$$

where G is the gravitational constant, γ is either the atmospheric specific heat C_a for a convective profile or $4R'$ for a radiative profile (R' is the modified gas constant) and T_n is the temperature at the base of the nearly isothermal outer layer, approximated here as the nebula temperature. The basal atmosphere temperature at the radius of the protoplanet r_p, is therefore

$$T_p = \frac{GM}{\gamma r_p} + T_n. \tag{9}$$

Hereafter, we identify T_p as the surface temperature, ignoring effects of boundary layers and departures from thermal equilibrium between atmosphere and the protoplanet surface. Assuming the lower layer of the atmosphere has a solar-type composition at all times, its major constituents being hydrogen and helium with the physical properties given in Table 1, surface temperatures during pebble accretion according to (9) are shown in Fig. 2 as functions of protoplanet mass.

The surface temperatures in Fig. 2 have large uncertainties (of order 25%), for several reasons. First, they are based on thermal equilibrium, which might not apply at times of very rapid accretion. Second, they assume uniform atmosphere luminosity. Consideration of pebble energetics (see Appendix) indicates that most of the pebble accretion energy is deposited in the lower atmosphere, rather than at the surface as uniform luminosity implies. Third, interactions between settling pebbles, the atmosphere, and the protoplanet interior modify the atmosphere composition, and thereby

Table 1
Pebble accretion properties.

Property	Notation	Value(s)
Earth mass, present	M_E	5.97×10^{24} kg
Solar mass	M_S	1.99×10^{30} kg
Seed mass, protoplanet	M_0	$1\times10^{-4}M_E$
Proto-Earth, Theia orbital radius	$\mathcal{R}$	1.5×10^{11} m
Proto-Earth, This orbital angular velocity	Ω	2×10^{-7} rad/s
Pebble Stokes number	St	0.1
Pebble headwind number	Z_{hw}	0.1
Pebble column density, t=0	Σ_0	0.2-0.3 kg/m^2
Solar nebula dissipation time scale	τ_n	3 Myr
Pebble accretion end time	$2\tau_n$	6 Myr
Solar nebula temperature	T_n	140 K
Core-forming metal fraction	μ	0.32 kg/kg
Mantle-forming silicate density	ρ_m	4×10^3 kg/m^3
Core-forming metal density	ρ_c	10×10^3 kg/m^3
Undifferentiated mixture density	ρ_u	4.95×10^3 kg/m^3
^{26}Al heat density, decay time	H_0, τ_{Al}	1×10^{-7} W/kg, 1.05 Myr
Atmosphere composition	H_2, He	0.854, 0.146 mol/mol
Atmosphere opacity	σ	0.1 m^2/kg
Atmosphere gas constant	R'	3.65×10^3 J/kg/K
Atmosphere specific heat	C_a	12.3×10^3 J/kg/K
Magma solidus, liquidus	T_{ms0}, T_{ml0}	1500, 1900 K
Magma melting coefficients	a_{ms}, a_{ml}	24, 25 K/GPa
Magma, mantle specific heats	C_m	1, 1.25×10^3 J/kg/K
Magma thermal expansion	α_{m0}, α'_m	2.7×10^{-5}/K, 1.65×10^{-2}/GPa
Mantle thermal expansion	$\alpha_{m0}/2$	1.35×10^{-5}/K
Magma thermal diffusivity	κ_m	1×10^{-6} m^2/s
Rheological transition temperature	T_{rt0}	1700 K
Core metal liquidus	T_{cl0}	1700 K
Core metal melting coefficients	a_{c1}, a_{c2}	19.5 K/GPa, -0.02 K/GPa^2
Core metal specific heat	C_c	0.85×10^3 J/kg/K
Core metal thermal expansion	α_c	1.5×10^{-5}/K
Undifferentiated specific heat	C_u	1.1×10^3 J/kg/K

Subscripts:
$E, S, Hill, p, hw, peb$ = Earth, Sun, Hill, protoplanet surface, headwind, pebble;
m, c, u, s, l, i = mantle & magma, core, undifferentiated, solidus, liquidus, internal;
$a, n, rt, Al, 0$ = atmosphere, nebula, rheological transition, ^{26}Al, initial & 1 bar.

modify its near-surface thermal structure. Possible modifications include a silicate vapor phase from pebble ablation (Brouwers et al., 2018), water vapor (Ida et al., 2019), and carbon dioxide (Johansen et al., 2021). The influence of these additional constituents on the surface temperature depends on their concentrations, which increase with increasing protoplanet mass.

For example, the partial pressure of silicate vapor at 3400 K is approximately 0.16 bar according to Visscher and Fegley (2013), barely 1% of the surface pressure in the radiative atmosphere above the $0.7M_E$ protoplanet (M_E denotes the present-day Earth mass). However, because of higher surface temperatures, the silicate vapor partial pressure becomes comparable to the surface atmosphere pressure on the $1M_E$ protoplanets in Fig. 2, for either atmosphere type. Accordingly, in this study our model Earths are constructed by merging protoplanets with final masses of $0.7M_E$ and smaller, in order to limit the effects of departures from thermal equilibrium and changes in atmosphere composition during the accretion process.

4. Internal structure

Fig. 3 shows internal structures of a hypothetical terrestrial protoplanet at four stages of pebble accretion: undifferentiated, two partially differentiated stages, and fully differentiated. All three densities are involved, ρ_u, ρ_m and ρ_c, arranged as shown in the figure. In the undifferentiated Stage 1, the protoplanet is a solid homogeneous mixture of metal and silicate components, and its temperature is dictated primarily by heating from ^{26}Al decay. The temperature at depth is higher than near the surface in this stage because radioactive heat has accumulated at depth over a longer

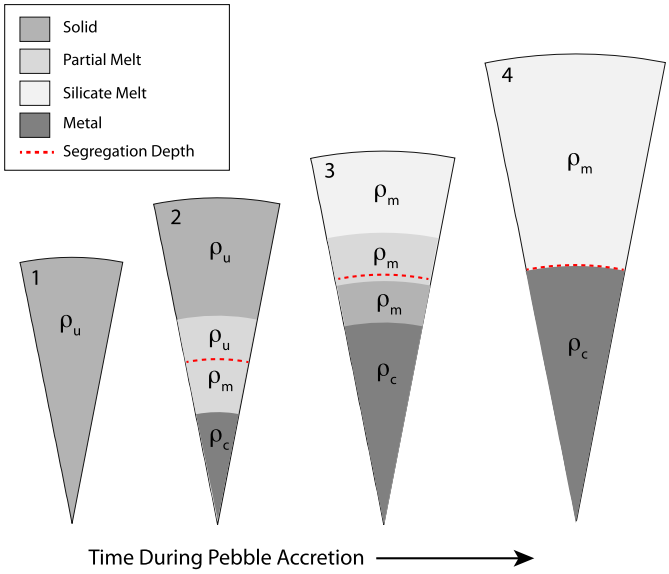

Fig. 3. Idealized stages in the evolution of a terrestrial protoplanet interior during pebble accretion. Shading indicates state (solid vs. partial melt vs. melt); ρ_m, ρ_c, and ρ_u denote mantle-forming silicate, core-forming metal, and undifferentiated densities, respectively. Dashed lines mark the depth of metal-silicate segregation at each stage.

time interval, so much so that the protoplanet begins to melt from the center outward.

Deep melting leads to the transient Stage 2 structure shown in Fig. 3, consisting of a small, segregated metallic core underlying a

layer of partially molten silicates drained of metals, above which is undifferentiated material, both partially molten and solid. The density stratification at this stage is unstable because $\rho_u > \rho_m$, signifying that an overturn of this structure is inevitable. Our model formulation does not include the dynamics of this overturn. Instead, we specify transition from Stage 2 at the time when the surface temperature reaches the silicate rheological transition temperature T_{rt}, indicating surface magma ocean conditions. At that point, metals accumulate in the surface magma ocean. Their excess density, coupled with the density deficit in the deep partially molten layer, implies overturn of the silicate-bearing layers and an adiabatic temperature variation with depth. The outcome is depicted in Stage 3 of Fig. 3. It consists of silicate melt (a surface magma ocean) overlying differentiated solid or partially molten silicate layers, plus a metallic core. This arrangement is similar to the structure predicted for the aftermath of a giant impact on a protoplanet without a blanketing atmosphere (Kendall and Melosh, 2016).

Stage 3 is also transient. The surface temperature continues to rise with time in proportion to the mass of the protoplanet. This temperature rise causes the depth of the magma ocean to increase, until it occupies the entire silicate part of the protoplanet. From that point on, the protoplanet consists of two differentiated, entirely molten layers: a global magma ocean overlying a liquid metallic core, as depicted in Stage 4 of Fig. 3. This configuration lasts as long as the thermal blanketing effect of the atmosphere remains and the protoplanet continues to grow through pebble accretion. Whether or not a terrestrial protoplanet passes through all four stages in Fig. 3 depends on the total mass of pebbles it acquires. As we show in the following Section, our calculations indicate that Stage 4 is accessed once the protoplanet mass reaches approximately $0.35 M_E$.

The pressure in the protoplanet interior P is determined from the hydrostatic balance

$$\frac{dP}{dr} = -\rho g, \tag{10}$$

in which ρ is the density appropriate to each region in Fig. 3, and g is internal gravity, given by

$$g = \frac{GM_i}{r^2}, \tag{11}$$

where M_i is the total mass inside radius r. For reference, using Table 1 values of ρ_m=4×10^3 kg/m^3, ρ_c=10×10^3 kg/m^3, and $\mu = 0.32$, a spherical $1 M_E$ protoplanet with these densities and metal fraction has a 6605 km surface radius, 9.14 m/s^2 surface gravity, and 108 GPa hydrostatic pressure at its 3574 km core-mantle boundary radius. In comparison to present-day Earth values, the model surface and core-mantle boundary radii are slightly higher and the model gravity and core-mantle boundary pressure are slightly lower, all qualitatively consistent with the very high temperature conditions implied by pebble accretion.

Differentiated and undifferentiated regions in the interior are identified by comparing model temperatures to melting temperatures at each depth. We use linear silicate solidus and liquidus temperature variations with the forms

$$T_{ms} = T_{ms0} + T'_{ms} P, \qquad T_{ml} = T_{ml0} + T'_{ml} P, \tag{12}$$

where the subscripts s and l refer to solidus and liquidus, respectively, T_{ms0} and T_{ml0} are standard (1 bar) pressure values, and T'_{ms} and T'_{ml} are their pressure derivatives. The values of the pressure derivatives in Table 1 are chosen so that (12) match the Andrault et al. (2011) chondritic melting curves at 70 GPa. Within partial melt regions, we assume that the silicate melt fraction f_m varies linearly between the solidus and liquidus, so that

$$f_m = \frac{T - T_{ms}}{T_{ml} - T_{ms}} \tag{13}$$

and f_m=1 for $T > T_{ml}$. We also specify the pressure dependence of the rheological transition temperature, above which the silicate partial melt loses strength and behaves like a low viscosity liquid in terms of its dynamics:

$$T_{rt} = T_{rt0} + T'_{rt} P, \tag{14}$$

in which $T_{rt0} = (T_{ms0} + T_{ml0})/2$ and $T'_{rt} = (T'_{ms} + T'_{ml})/2$. According to (13) and (14), the silicate melt fraction is $f_m = 0.5$ at the rheological transition. For core-forming metals, we adopt a linear melting law of the form

$$T_{cl} = T_{cl0} + T'_{cl} P. \tag{15}$$

The values for T_{cl0} and T'_{cl} in Table 1 are derived from iron melting temperatures by Anzellini et al. (2013), in which we have included a small melting point reduction due to the presence of light elements. Effects of eutectic melting are not considered here.

The thermal structures assigned to the interior regions in Fig. 3 depend on the dominant mode of heat transfer in each region. In undifferentiated material, where $T < T_{rt}$, heat transfer is too slow in the first few million years to balance the heat produced by ^{26}Al decay. Accordingly, for this material we assume it accretes at the surface temperature and its temperature increases with time according to

$$\frac{\partial T}{\partial t} = \frac{H(t)}{C_u} \tag{16}$$

where

$$H(t) = H_0 \exp(-t/\tau_{Al}) \tag{17}$$

is the heat production rate from ^{26}Al decay, H_0 is its initial (t=0) value, τ_{Al} is its decay rate, and C_u is the specific heat of the undifferentiated solid. The partial derivatives in (16) signify that the temperature increase applies at fixed radius. The seed temperature profile is calculated the same way, assuming the seed radius increased linearly with time starting at t=0.

Differentiated regions are identified by temperatures having exceeded the rheological transition, that is, where $T > T_{rt}$. At the point in time and depth where this inequality is first met, the density is reduced from ρ_u to ρ_m, its metal content is transferred to the core, and the core radius is increased by the appropriate amount. In all such differentiated regions we apply adiabatic thermal profiles, on the assumption that thermal advection is the dominant mode of heat transfer. Justification for this assumption is given in the Appendix.

Adiabatic temperature profiles are determined in solid and liquid silicate and in liquid metal regions using

$$\frac{dT}{dP} = \frac{\alpha T}{\rho C}, \tag{18}$$

where α is thermal expansivity, ρ is density, C is specific heat for each material. For liquid metal and solid silicate we use constant values of α given in Table 1. For liquid silicate regions, where $T > T_{ml}$, there is a strong pressure effect on thermal expansion (de Koker and Stixrude, 2009). Accordingly, we adopt a pressure variation of the form

$$\alpha_m = \frac{\alpha_{m0}}{1 + \alpha'_m P} \tag{19}$$

where α_{m0} and α'_m are constant factors, their values given in Table 1. In silicate partial melt regions, where $T_{ms} < T < T_{ml}$,

the adiabatic temperature gradient is anomalous because of phase changes (Solomatov, 2015). In those regions we adopt an adiabatic temperature variation given by

$$\frac{dT}{dP} = \frac{T'_{ms} + T'_{ml}}{3}. \tag{20}$$

Temperature continuity with the atmosphere is enforced at the protoplanet surface and between regions in the interior. Thermal boundary layers and stratified regions are ignored on the assumption they are thin. Some regions classified as silicate partial melt may at the same time be classified as undifferentiated for purposes of density, while others may be differentiated yet solid. However, because temperatures rise very quickly during pebble accretion, such regions are both localized in depth and short-lived in time, existing only briefly over limited depth regions during portions of Stages 2 and 3. Consequently, they have only minor effects on overall model behavior.

Important diagnostics for pebble accretion are the pressures and temperatures where core-forming metals segregate from silicates. Here, we define core segregation as the final contact between metal and silicates. If metal pebbles are free to descend through molten or partially molten silicate without aggregating into a larger mass, then according to our definition, metal-silicate segregation occurs at the temperature and pressure of the core-mantle boundary. Alternatively, if the silicate has the strength to arrest pebble descent, such as at the base of a magma ocean, metal-rich layers will accumulate at those locations. These layers then undergo Rayleigh-Taylor instability (Stevenson, 1990), forming metal diapirs large enough to sink through partially molten or solid silicate and merge with the core. The significance here is that, once large metal diapirs form, most of that metal has effectively segregated, at least insofar as its ability to interact with silicates as it descends toward the core.

To enforce our definition of core segregation, we adopt the following logic. If temperatures in the radial interval separating undifferentiated material and the core-mantle boundary are everywhere equal to or higher than the rheological transition, then the segregation conditions are the core-mantle boundary pressure and temperature at that time. This is the situation for pebbles entering a whole-mantle magma ocean or a basal magma ocean. Alternatively, if the temperature profile lies below the rheological transition somewhere in that radial interval, then the segregation conditions are those corresponding to the pressure and temperature at the transition. This is the situation for a magma ocean that extends downward only partway through the silicate portion of the protoplanet, which is a commonly assumed configuration during Earth accretion (Elkins-Tanton, 2012).

5. Model results

Fig. 4 shows the results of building a $0.7M_E$ protoplanet by pebble accretion, using the properties from Table 1 in equations (4)-(20). Panel a in Fig. 4 shows the time history of the pebble column density Σ, the pebble settling rate F and the protoplanet mass M. The pebble column density is normalized by its initial value (0.205 kg/m^2), the pebble settling rate by its maximum value, and protoplanet mass by M_E. The vertical dotted line indicates the time when the seed, with initial mass $10^{-4}M_E$, begins to acquire pebbles in the Hill regime. The pebble column density decreases rapidly with time, falling to a few percent of its initial value by 6 Myr. In contrast, the pebble settling rate first increases with time, reaching its maximum around 2.5 Myr, then decreases rapidly. The initial rise in pebble settling is due to the rapid increase in protoplanet mass, which greatly enlarges the settling cross-section. Only after the pebble column density falls below 50% of its initial value does the settling rate decrease substantially.

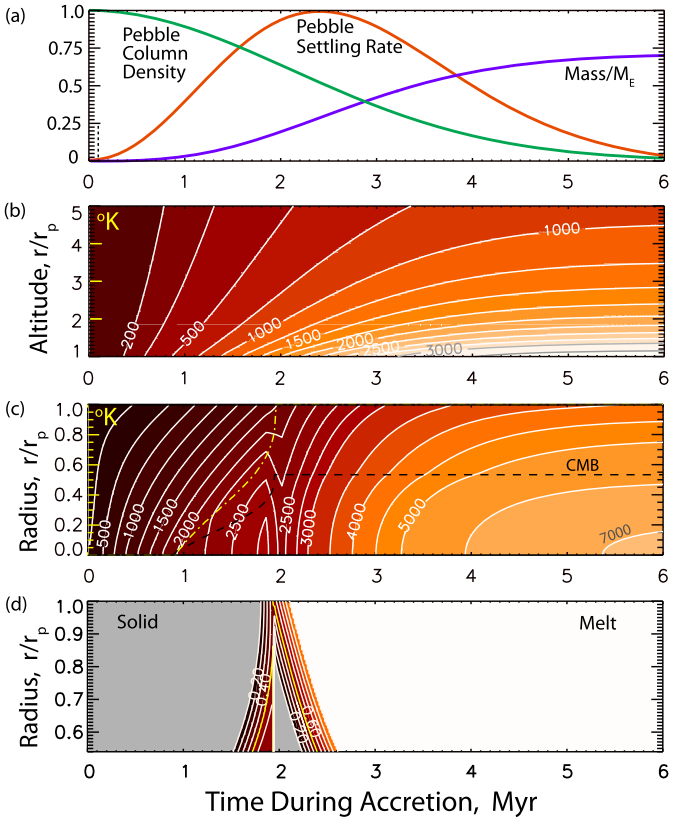

Fig. 4. Time evolution of the growth of a $0.7M_E$ protoplanet by pebble accretion with a convective nebular atmosphere. (a) Pebble column density and pebble settling rate normalized by their maximum values, and protoplanet mass relative to present-day Earth; (b) Atmosphere temperature versus altitude normalized by protoplanet radius; (c) Interior temperature versus normalized radius. Dash and dash-dot curves mark the core-mantle boundary and differentiation radii, respectively; (d) Silicate melt fraction versus normalized radius. Gold contours (0.5 melt fraction) mark the silicate rheological transition. The silicate melt distribution is inverted at 1.9 Myr by the adiabatic overturn event.

The second panel, Fig. 4b, shows temperatures the lower portion of the nebular atmosphere, assuming a convective thermal profile. Starting from the nebula temperature, the atmosphere rapidly heats up as it deepens, with the surface atmosphere temperature approaching 3800 K toward the end of pebble accretion. At this temperature the equilibrium silicate vapor pressure is about 2 bars (Visscher and Fegley, 2013) compared to the surface hydrostatic pressure of about 30 bars.

The third and fourth panels in Fig. 4 show the thermal evolution of the protoplanet interior. Fig. 4c shows the distribution of temperature throughout the interior, whereas Fig. 4d shows the distributions of solid, melt, and partial melt in the region $0.55 < r/r_p < 1$, the post-accretion silicate portion of the protoplanet. Together these two panels illustrate the four stages of protoplanet growth depicted in Fig. 3. In the initial Stage 1 the protoplanet is solid throughout, with a thermal gradient governed by the heat produced by ^{26}Al decay. The partially differentiated Stage 2 begins near 0.9 Myr, when the central temperature exceeds the rheological transition at that pressure. This transition is marked by the inflection points of the dashed and dash-dot curves in Fig. 4c, which show the relative depths of the metallic core (labeled CMB) and the differentiated portion of the protoplanet, respectively. Stage 2 lasts approximately 1 Myr in Fig. 4, that is, between 0.9 and 1.9 Myr. During this time, melting progresses upward, with differentiation approaching $0.54r_p$, the final core-mantle boundary radius ratio, around 1.6 Myr and reaching the surface around 1.9 Myr.

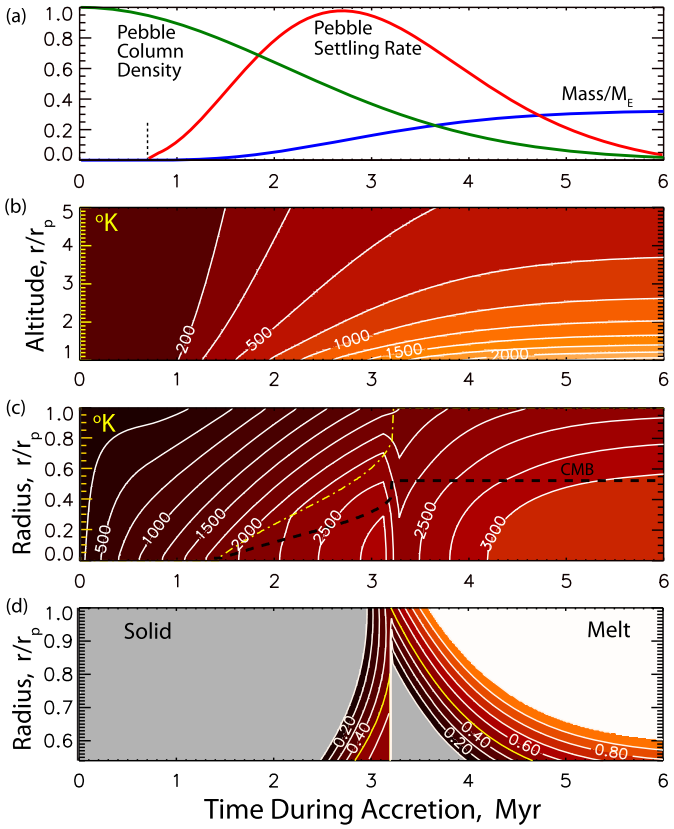

Fig. 5. Time evolution of the growth of a $0.31M_E$ model protoplanet by pebble accretion with a convective nebular atmosphere. (a) Pebble column density and pebble settling rate normalized by their maximum values, and protoplanet mass relative to present-day Earth; (b) Atmosphere temperature versus altitude normalized by protoplanet radius; (c) Interior temperature versus normalized radius. Dash and dash-dot curves mark the core-mantle boundary and differentiation radii, respectively; (d) Silicate melt fraction versus normalized radius. Gold contours (0.5 melt fraction) mark the silicate rheological transition.

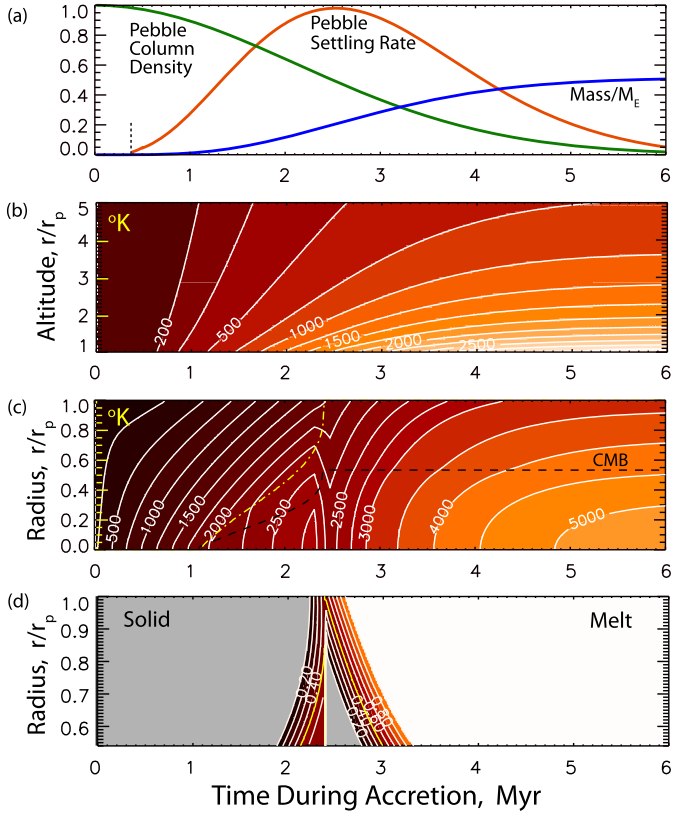

Fig. 6. Time evolution of the growth of a $0.505M_E$ model protoplanet by pebble accretion with a convective nebular atmosphere. (a) Pebble column density and pebble settling rate normalized by their maximum values, and protoplanet mass relative to present-day Earth; (b) Atmosphere temperature versus altitude normalized by protoplanet radius; (c) Interior temperature versus normalized radius. Dash and dash-dot curves mark the core-mantle boundary and differentiation radii, respectively; (d) Silicate melt fraction versus normalized radius. Gold contours (0.5 melt fraction) mark the silicate rheological transition.

Once the surface temperature exceeds T_{rt}, the model transitions from Stage 2 to Stage 3, marked in Fig. 4d by an inversion of the mantle structure, with silicate liquid overlying differentiated silicate partial melt overlying a basal silicate layer that is also differentiated but solidified by adiabatic compression. From the beginning of Stage 3 on, the relative depth of the core-mantle boundary remains constant and no undifferentiated material remains in the interior, as indicated by the flat segment of the CMB curve in Fig. 4c. However, internal temperatures continue to increase during Stage 3 because the adiabatic thermal profiles in silicate and metallic regions are coupled to the rising surface temperature. In consequence, the surface magma ocean rapidly deepens, the rheological transition reaching the core-mantle boundary around 2.4 Myr. From 2.6 Myr to the end of pebble accretion the entire protoplanet is molten.

Figs. 5 and 6 show the results of building smaller protoplanets by pebble accretion, using the same nebular environment and pebble properties as in Fig. 4. In Fig. 5 a $10^{-4}M_E$ seed mass begins accreting pebbles at 0.7 Myr and reaches a final mass of $0.31M_E$, whereas in Fig. 6 pebble accretion onto the same seed mass begins at 0.35 Myr and the final mass is $0.505M_E$ These starting times were chosen in order to produce two-body masses comparable to the present-day Earth-Moon system. Specifically, by merging the accreted protoplanets in Figs. 4 and 5 we model the collision of a larger proto-Earth and a smaller Theia (Ćuk and Stewart, 2012), yielding the approximate Earth-Moon system mass. Similarly, the same final system mass is obtained by merging two of the protoplanets in Fig. 6, a model for the equal mass collision scenario (Canup, 2012).

Panel a in Fig. 5 shows the same general behavior in terms of pebble settling and protoplanet mass as in Fig. 4, except that pebble settling starts later in time in Fig. 5 and the final mass is less. The reduced mass limits the growth of the nebular atmosphere, and as shown in Fig. 5b, the blanketing effect in this case is weaker, such that the final surface temperature barely exceeds 2400 K. The weaker thermal blanketing by the atmosphere strongly affects the evolution of the protoplanet interior, as shown in Figs. 5c and 5d. Differentiation and core segregation are delayed in this case, and the internal temperatures are relatively low, such that the core-mantle boundary temperature is only slightly above 3000 K at the end of pebble accretion. More significantly, Fig. 5d shows that the protoplanet never entirely melts in this case (i.e., the evolution does not reach Stage 4). At the end of pebble accretion magma ocean includes a basal a partial melt, although its temperature is everywhere above the rheological transition.

The evolution shown in Fig. 6 for the $0.505M_E$ protoplanet is intermediate between Figs. 4 and 5. All four evolutionary stages are present in this case, but Stages 2-4 occur later in time compared to Fig. 4. Likewise, the surface and core-mantle boundary temperatures are more moderate compared to Fig. 4. In short, in spite of some differences in their overall evolution, in each of these cases the core is predicted to fully segregate while pebble accretion is active, although under somewhat different temperature and pressure conditions.

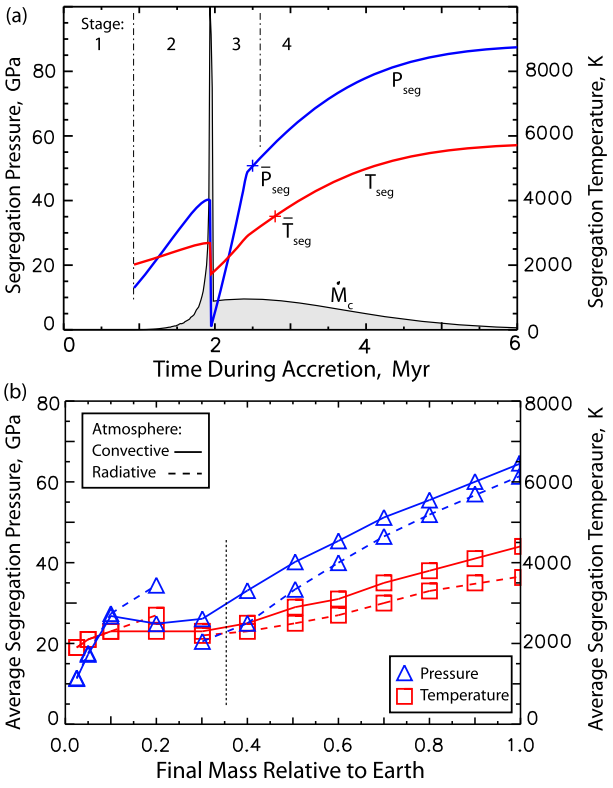

Fig. 7. a: Core segregation pressure and temperature conditions versus time from the $0.7M_E$ pebble accretion case illustrated in Fig. 4. The curve labeled $\dot{M}_c$ is the normalized mass flux into the core. $\bar{P}$ and $\bar{T}$ are averages computed using equation (21). Stages 1-4 are those illustrated in Fig. 3. b: Average core segregation pressure and temperature versus final protoplanet mass, for convective and radiative nebular atmospheres. To the right of the dotted vertical line, protoplanets evolve to the fully molten Stage 4 structure.

Fig. 7a shows core segregation temperature, pressure, and mass flux into the core versus time from the $0.7M_E$ pebble accretion case illustrated in Fig. 4. The core mass flux $\dot{M}_c$ spikes upward at the time of the overturn event, then progressively decreases as the accretion rate diminishes. Segregation pressure and temperature (P_{seg}, T_{seg}) variations show the inverse behavior, spiking downward during overturn, then progressively increasing after that. Also shown are time averages of the segregation conditions, defined as

$$(\bar{P}_{seg}, \bar{T}_{seg}) = \frac{1}{M_c} \int_{t=0}^{6Myr} (P_{seg}, T_{seg}) \dot{M}_c dt, \qquad (21)$$

M_c here denoting the (final) core mass at 6 Myr. The average segregation pressure and temperature are about 60% of their final values, consistent with other continuous or multi-stage core formation models (Siebert et al., 2012).

Fig. 7b shows average segregation pressure and temperature versus final protoplanet mass, for both convective and radiative atmospheres. As expected, the average segregation pressures and temperatures are somewhat higher beneath a convective atmosphere, compared to beneath a radiative atmosphere, although for most final masses these differences are not particularly large. Exceptions are found around $0.2M_E$ in Fig. 7b, corresponding to the mass interval in which pebble accretion ends while the protoplanet lies in evolution Stages 2 and 3 of Fig. 3. As the protoplanet evolves into Stage 4, metal-silicate segregation occurs at the core-mantle boundary, and the average segregation pressure and temperature increase systematically with protoplanet mass for both atmosphere types, as indicated by the curves to the right of the vertical dotted line in Fig. 7b.

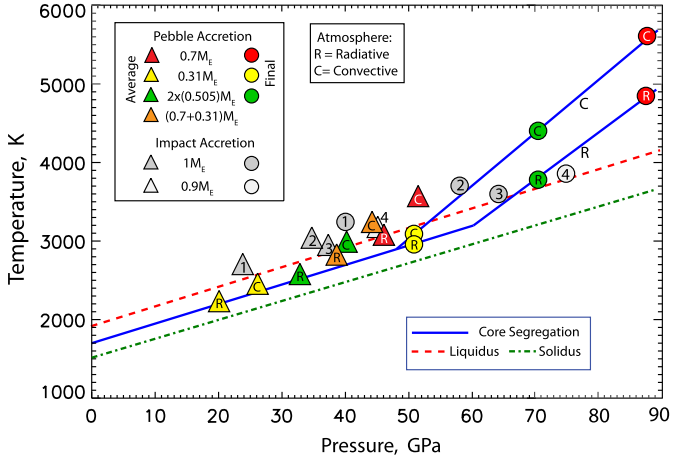

Fig. 8. Pebble accretion model results for core segregation (solid curves=pressure-temperature conditions; circles=final or maximum values; triangles=averages) compared to pressure-temperature conditions from impact-driven multi-stage or continuous core segregation models constrained by metal-silicate partitioning of siderophile elements. 1=Wood et al., 2006; 2=Siebert et al., 2012 intermediate geotherm; 3=Badro et al., 2015 cool geotherm; 4=Rubie et al., 2015 planetesimals + embryos. Dashed and dash-dot curves are our model silicate liquidus and solidus; C and R denote convective and radiative atmospheres. Final protoplanet masses are indicated in the label.

6. Comparison with impact-based core segregation

Fig. 8 compares core segregation conditions from our pebble accretion model to the segregation conditions from accretion models based on large impacts and constrained by metal-silicate partitioning of siderophile elements. The two dashed curves are our model silicate solidus and liquidus. The solid blue curves are our model segregation conditions for radiative and convective atmospheres (labeled R and C, respectively), and the triangles and circles are averages and final (maximum) values, respectively, of these conditions for various protoplanets. The orange triangles in Fig. 8 are two-body averages of the $0.7M_E$ and $0.31M_E$ protoplanets (i.e., averages of the red and yellow triangles). This simulates the merger of a larger proto-Earth and a smaller Theia, in which the cores of Theia and the proto-Earth are combined without interacting with the silicates. In the same way, the green triangles in Fig. 8 simulate the merger of proto-Earth and Theia with identical masses.

At lower pressure and temperature, the trajectory of our segregation curve in Fig. 8 follows the rheological transition, where we have assumed that metals freely segregate. The average segregation conditions for the $0.31M_E$ protoplanet lie below our model silicate liquidus, as do their final segregation conditions, indicating that most of the metal segregated from partially molten silicate at the rheological transition in these cases. In contrast, for the $0.7M_E$ protoplanets, the final and the average segregation conditions lie above the liquidus. Although some segregation occurs at the rheological transition in these cases, additional segregation occurs at higher temperatures, including above our model silicate liquidus. These high temperature conditions are indicated by the segregation curves labeled C and R in Fig. 8, and correspond to evolution Stage 4 in which small metal volumes fall through silicate magma directly into the core.

The gray symbols in Fig. 8 are a sampling of results from impact-based accretion models constrained by metal-silicate partitioning data on siderophile elements, from Wood et al. (2006), Siebert et al. (2012), Badro et al. (2015), and Rubie et al. (2015).

These models assume either a sequence or a continuous distribution of large impacts, producing a magma ocean whose variable depth defines a segregation pressure curve. Segregation temperatures are usually assumed to lie along the mantle liquidus, with a variety of mantle liquidus profiles being considered. Final segregation conditions from these models are denoted by gray circles in Fig. 8; the corresponding average segregation conditions (gray triangles) were calculated using 60% of the final segregation pressures.

The average segregation conditions from our pebble accretion model are in broad agreement with the average segregation conditions from the impact-based models, especially the mergers of protoplanets pebble-accreted under convective atmospheres. This is perhaps surprising, given the fundamental differences in the two accretion mechanisms. However, some of these differences complement each other. For example, our pebble accretion model segregates at the core-mantle boundary, whereas impact-based models typically segregate at mid-mantle depths. But because segregation under pebble accretion operates when protoplanets are relatively small, the pressure-temperature conditions at the core-mantle boundary are similar to the mid-mantle in a larger body built by impacts.

7. Summary

Pebble accretion is a relatively straightforward planet formation mechanism, in that only three main ingredients are needed: a large population of pebbles, nebular gas, and a seed mass. Once these are in place, core segregation proceeds deterministically, on a schedule dictated by the evolution of the protoplanetary disk.

Pebble accretion has multiple implications for core formation in the Earth. It is global in scale, drawing solids and gas from diverse parts of the protoplanetary environment. It synchronizes core segregation to the accretion rate on timescales of a few million years. And it implies pervasive melting and high temperature metal-silicate segregation, thereby offering new ways to interpret mantle siderophile abundances.

In terms of modeling core formation under pebble accretion, there is much room for extensions and improvements. Better constraints are needed on disk properties such as pebble composition and density, Stokes and headwind numbers, and orbital variations. In addition, more realistic models should include full compressibility, redox reactions, better melting laws, atmosphere constituents such as silica and water vapor, as well as the effects of oxygen fugacity, density stratification, and larger impacts.

CRediT authorship contribution statement

Peter Olson: Conceptualization, Theory, Software Development, Graphics, Writing. **Zachary Sharp:** Conceptualization, Writing-Reviewing-Editing, Literature Search. **Susmita Garai:** Methods, Software Development, Graphics.

Declaration of competing interest

The authors declare that they have no known competing financial interests or personal relationships that could have appeared to influence the work reported in this paper.

Acknowledgements

This work was supported by grant EAR1953992 from the National Science Foundation.

Appendix A

A.1. Pebble trajectories

Pebbles in a protoplanetary disk are subject to gravitational attraction and nebular gas drag. In an orbiting reference frame with a protoplanet at the origin, the motions of small nearby pebbles consist of headwind, crosswind, Keplerian shear, and acceleration toward the protoplanet. Neglecting crosswind for now, the nondimensional pebble velocity components in this reference frame are (Ormel and Klahr, 2010)

$$v_y = -\frac{3ySt}{r^3} - \frac{Z_{hw}}{1+St^2} - \frac{3x}{2}; \qquad v_x = -\frac{3xSt}{r^3}, \tag{A.1}$$

where y is the coordinate tangent to the orbital direction, x is the radial coordinate, St and Z_{hw} are the pebble Stokes and headwind numbers (assumed constant), and $r^2 = x^2 + y^2$. In (A.1) the velocity components are nondimensionalized by the product of the Hill radius r_{Hill} and orbital angular velocity Ω. The first term in both v_y and v_x represents the gravitational attraction by the protoplanet, and the second term in v_y represents a uniform headwind. The third term in v_y represents Keplerian shear. A modification of (A.1) that includes crosswind is given below.

Pebble trajectories based on (A.1) are defined (to order St^2) by

$$\frac{dy}{dx} = \frac{v_y}{v_x} = \frac{y}{x} + \frac{Z_{hw} r^3}{3xSt} + \frac{r^3}{2St}. \tag{A.2}$$

Using $y = x\tan\theta$, (A.2) becomes

$$\cos\theta \frac{d\theta}{dx} = \frac{Z_{hw} x}{3St} + \frac{x^2}{2St}, \tag{A.3}$$

which integrates to yield

$$x^3 + Z_{hw}x^2 - \left(6St(\sin\theta - 1) + {x_0}^3 + Z_{hw}{x_0}^2\right) = 0, \tag{A.4}$$

where x_0 is the starting x-value of the trajectory. The positive x_0-value that divides pebble settling from pebble escape, x_{crit}, is obtained by requiring that $\theta = -\pi/2$ as $x \to 0$, which leads to the following cubic equation

$${x_{crit}}^3 + Z_{hw}{x_{crit}}^2 - 12St = 0. \tag{A.5}$$

The positive real root of (A.5) corresponds to the critical trajectory approaching from positive x and y. For $St = Z_{hw} = 0.1$, $x_{crit} \simeq 1.03$, meaning that for these parameters, the pebble capture radius is very nearly the Hill radius. The pebble trajectories approaching the protoplanet from the right in Fig. 1 are constructed by starting at positive x_0 and y =3, and marching in increments of decreasing θ, using (A.4) to reach the origin. Pebble trajectories approaching from the left in Fig. 1 were started from negative x_0 and y =-3.

We can factor in the effects of a crosswind, representing pebble drift in the negative x-direction (toward the Sun), by rotating trajectories. Adding a uniform crosswind, the dimensionless velocity components (A.1) in the far-field (large r limit) are

$$v_y = -\frac{Z_{hw}}{1+St^2} - \frac{3x}{2}; \qquad v_x = -\frac{2Z_{hw}St}{1+St^2}. \tag{A.6}$$

We rotate the velocity components in (A.6) through an angle β given by

$$\beta \simeq \tan^{-1}\left(\frac{2Z_{hw}St}{Z_{hw} + a(1+St^2)}\right), \tag{A.7}$$

with $a = \pm 3/4$, depending on the sign of x. The result of this rotation is a modified far-field velocity $v_{y'}$ that absorbs most of the crosswind.

The dimensionless pebble settling rate is given by

$$F^* = \int_{-x'_{crit}}^{0} v_{y'} dx' - \int_{0}^{+x'_{crit}} v_{y'} dx', \tag{A.8}$$

where the primes denote the rotated coordinates. For $St = Z_{hw} = 0.1$, (A.8) yields $F^* \simeq 2$, and in terms of dimensional quantities the two-dimensional pebble settling rate (mass flux) becomes

$$F \simeq 2 r_{Hill}^2 \Omega \Sigma, \tag{A.9}$$

where Σ is pebble column density. According to (A.6), the cross-wind correction to $v_{y'}$ is of order St. The rotation angle β is small in this case, of order 5 degrees. The largest errors come from rotating the shear term in (A.6), and amount to a few percent error in F.

A.2. Nebular atmosphere structure

We assume the lower atmosphere is in statistical thermal equilibrium, is an ideal gas with uniform opacity, and with total luminosity (total heat flux) approximately uniform with altitude. This latter condition assumes that settling pebbles deposit their accretion energy near the surface, rather than throughout the entire atmosphere. The governing equations consist of the hydrostatic balance, the ideal gas law, and a radiative thermal balance:

$$\frac{dP}{dr} = -\frac{\rho G M}{r^2}, \qquad P = \rho R' T, \qquad \frac{dT^4}{dr} = -\frac{3\sigma\rho L}{16\pi k r^2}. \tag{A.10}$$

Here P, ρ, and T are atmosphere pressure, density, and temperature, M is protoplanet mass, r is radial distance from its center, σ is atmosphere opacity, L is total luminosity, and k, R', and G are the Stefan-Boltzmann, modified gas, and gravitational constants. Integration of (A.10) yields, for the state variables

$$T = \frac{GM}{4R'r} + T_n, \qquad P = \frac{16\pi k G M}{3\sigma L} T^4, \qquad \rho = \frac{16\pi k G M}{3\sigma L R'} T^3, \tag{A.11}$$

where T_n is the far field temperature, here equated to the nebula temperature. In deriving (A.11) we have ignored terms of order $(T_n/T)^2$ and smaller. These formulas apply to a radiative thermal gradient; for an adiabatic thermal gradient, the specific heat C_a replaces R' in T. Note that, because of model assumptions, atmosphere pressure and density in (A.11) depend on total luminosity. They also depend on the accretion rate $\dot{M}$, because the accretion energy $GM\dot{M}/r_p$ makes the largest contribution to the total luminosity. In contrast, the atmosphere temperature in (A.11) depends on protoplanet mass but is independent of accretion rate.

A.3. Pebble energetics

The above formulas allow estimating the velocity of pebbles on surface impact. With quadratic drag (which controls pebble velocity near the surface) the stopping time of a spherical pebble is given by

$$\tau_d = \frac{6\rho_{peb} r_{peb}}{\rho v_{peb}}. \tag{A.12}$$

In (A.12), the subscripts peb refer to pebble properties, and ρ_{peb}, r_{peb}, and v_{peb} are their density, radius, and velocity relative to the gas. The terminal velocity of a pebble just above the surface is $v_{peb} = g'\tau_d$, where $g' = g(\rho_{peb} - \rho)$ is the reduced gravity of the pebble in the gas. In terms of these properties, the Stokes number of the pebble in the nebula can be written

$$St = \frac{\sqrt{2\pi}\,\rho_{peb} r_{peb}}{\Sigma_g} \tag{A.13}$$

where Σ_g is the column density of the nebular gas. Combining (A.12) - (A.13) and solving for the pebble terminal velocity yields

$$v_{peb} = \left(\frac{6 g' \Sigma_g St}{\sqrt{2\pi}\,\rho} \right)^{1/2}. \tag{A.14}$$

For a $0.5 M_E$ protoplanet with properties in Table 1, our accretion model gives g =7.25 m/s^2 for surface gravity, and (A.11) gives ρ=0.04 kg/m^3 for density at the convective atmosphere base. Using $St = 0.1$ and assuming a nominal Σ_g=1000 kg/m^2 gives $v_{peb} \simeq 200$ m/s for the pebble terminal velocity above the protoplanet surface. This is to be compared with the escape velocity under the same conditions, $v_{esc} = \sqrt{2GM/r_p} \simeq 8700$ m/s. Accordingly, the ratio of kinetic energy deposited by an impacting pebble to its accretion energy is less than 10^{-3}, implying that pebbles deposit very little of their accretion energy on surface impact. Nearly all of their accretion energy is converted to heat in the lower part of the atmosphere.

Settling pebbles contribute energy to the protoplanet interior primarily in three forms: radioactive heat, sensible heat, and segregation heat (Olson and Sharp, 2022). Radioactive heating given by (16) and (17) and deep melting dominate the first stage of pebble accretion, but become secondary once surface melting begins. For the pebble accretion case illustrated in Fig. 4, accretion supplies 6.3×10^{17} W on average to the atmosphere. In the interior, sensible heat from pebble settling supplies 4.9×10^{16} W and heat from metal segregation supplies 6.3×10^{16} W. Meanwhile the interior absorbs 1.1×10^{17} W of sensible heat on average. Therefore, to maintain thermal equilibrium, approximately 2×10^{15} W is transported from the interior to the surface in time average. For comparison, the heat loss by conduction down the magma adiabat is less than 10^{13} W. This discrepancy implies that the magma ocean is convective in time average, and unless stabilizing compositional variations exist, tends toward adiabatic except in thin boundary layer regions. A parallel energy analysis indicates that convection is somewhat less likely in proto-core. However, because its temperature profile is largely controlled by influx of heated metals and adiabatic compression, it too is expected to remain close to adiabatic.

References

Andrault, D., Bolfan-Casanova, N., Lo Nigro, G., Bouhifd, M.A., et al., 2011. Solidus and liquidus profiles of chondritic mantle: implication for melting of the Earth across its history. Earth Planet. Sci. Lett. 304, 251–259.

Andrews, S.M., 2015. Observations of solids in protoplanetary disks. Publ. Astron. Soc. Pac. 127, 961–993.

Ansdell, M., Williams, J.P., Van der Marel, N., Carpenter, J.M., et al., 2016. ALMA survey of Lupus protoplanetary disks. I. Dust and gas masses. Astrophys. J. 828, 46.

Anzellini, S., Dewaele, A., Mezouar, M., et al., 2013. Melting of iron at Earth's inner core boundary based on fast X-ray diffraction. Science 340, 464–467.

Badro, J., Brodholt, J.P., Piet, H., et al., 2015. Core formation and core composition from coupled geochemical and geophysical constraints. Proc. Natl. Acad. Sci. 112 (40), 12310–12314.

Bottke, W.F., Walker, R.J., Day, J.M.D., Nesvorny, D., Elkins-Tanton, L., 2010. Stochastic late accretion to Earth, the Moon, and Mars. Science 330, 1527–1530.

Brouwers, M.G., Vazan, A., Ormel, C.W., 2018. How cores grow by pebble accretion. I. Direct core growth. Astron. Astrophys. 611, A65.

Canup, R.M., 2012. Forming a Moon with an Earth-like composition via a giant impact. Science 338, 1052–1055.

Carasco-González, C., Sierra, A., Flock, M., Zhu, Z., et al., 2019. The radial distribution of dust particles in the HL Tau disk from ALMA and VLA observations. Astrophys. J. 883, 71.

Clesi, V., Monteux, J., Qaddah, B., Le Bars, M., Wacheul, J.-B., Bouhifd, M., 2020. Dynamics of core-mantle separation: influence of viscosity contrast and metal/silicate partition coefficients on the chemical equilibrium. Phys. Earth Planet. Inter., 106547.

Ćuk, M., Stewart, S.T., 2012. Making the Moon from a fast-spinning Earth: a giant impact followed by resonant despinning. Science 338, 1047–1052.

de Koker, N., Stixrude, L., 2009. Self-consistent thermodynamic description of silicate liquids, with application to shock melting of MgO periclase and $MgSiO_3$ perovskite. Geophys. J. Int. 178, 162–179.

Elkins-Tanton, L.T., 2012. Magma oceans in the inner solar system. Annu. Rev. Earth Planet. Sci. 40, 113–139.

Eriksson, L.E.J., Johansen, A., Liu, B., 2020. Pebble drift and planetesimal formation in protoplanetary disks with imbedded planets. Astron. Astrophys. 635, A110.

Fischer, R.A., Campbell, A.J., Ciesla, F.J., 2017. Sensitivities of Earth's core and mantle composition to accretion and differentiation processes. Earth Planet. Sci. Lett. 458, 252–262.

Fleck, J.R., Rains, C.L., Weeraratne, D.S., Nguyen, C.T., Brand, D.M., et al., 2018. Iron diapirs entrain silicates to the core and initiate thermochemical plumes. Nat. Commun. 9, 71. https://doi.org/10.1038/s41467-017-02503-2.

Ida, S., Tamamura, T., Okuzumi, S., 2019. Water delivery by pebble accretion to rocky plants in habitable zones in evolving disks. Astron. Astrophys. 624, A28.

Ikoma, M., Genda, H., 2006. Constraints on the mass of a habitable planet with water of nebular origin. Astrophys. J. 648, 696–706.

Johansen, A., Lambrechts, M., 2017. Forming planets via pebble accretion. Annu. Rev. Earth Planet. Sci. 45, 359–387.

Johansen, A., Ronnet, T., Bizzarro, M., Schiller, M., et al., 2021. Pebble accretion model for the formation of the terrestrial planets in the solar system. Sci. Adv. 7, eabc0444.

Kendall, J.D., Melosh, H.J., 2016. Differentiated planetesimal impacts into a terrestrial magma ocean: fate of the iron core. Earth Planet. Sci. Lett. 448, 24–33.

Kleine, T., Walker, R.J., 2017. Tungsten isotopes in planets. Annu. Rev. Earth Planet. Sci. 45, 389–417.

Lambrechts, M., Johansen, A., 2012. Rapid growth of gas-giant cores by pebble accretion. Astron. Astrophys. 544, 13 pp.

Landeau, M., Deguen, R., Phillips, D., Neufeld, J.A., Lherm, V., Dalziel, S.B., 2021. Metal-silicate mixing by large Earth-forming impacts. Earth Planet. Sci. Lett. 564, 116888.

Levison, H.F., Kretke, K.A., Walsh, K.J., et al., 2015. Growing the terrestrial planets from the gradual accumulation of sub-meter-sized objects. Proc. Natl. Acad. Sci. USA 112. https://doi.org/10.1073/pnas.1513364112.

Monteux, J., Ricard, Y., Coltice, N., Dubuffet, F., Ulvrova, M., 2009. A model of metal-silicate separation on growing planets. Earth Planet. Sci. Lett. 287, 353–362.

Morbidelli, A., Lambrechts, M., Jacobson, S., Bitsch, B., 2015. The great dichotomy of the Solar System: small terrestrial embryos and massive giant planet cores. Icarus 258, 418–429.

Nimmo, F., Kretke, K., Ida, S., et al., 2018. Transforming dust to planets. Space Sci. Rev. 214. https://doi.org/10.1007/s11214-018-0533-2.

Olson, P.L., Sharp, Z.D., 2022. Primordial helium-3 exchange between Earth's core and mantle. Geochem. Geophys. Geosyst. 23, e2021GC009985.

Ormel, C.W., Klahr, H.H., 2010. The effect of gas drag on the growth of protoplanets. Analytical expressions for the accretion of small bodies in laminar disks. Astron. Astrophys. 520, A43.

Pérez, L.M., Chandler, C.J., Isella, A., Carpenter, J.M., Andrews, S.M., 2015. Grain growth in the circumstellar disks of the young stars CY Tau and DoAr 25. Astrophys. J. 813, 41.

Popovas, A., Nordlund, A., Ramsey, J.P., Ormel, C.W., 2018. Pebble dynamics and accretion on to rocky planets - I. Adiabatic and convective models. Mon. Not. R. Astron. Soc. 479, 5136–5156.

Powell, D., Murray-Clay, R., Perez, L.M., Schlichting, H.E., Rosenfeld, M., 2019. New constraints from dust lines on the surface densities of protoplanetary disks. Astrophys. J. 878, 116.

Rubie, D., Jacobson, S.A., 2016. Mechanisms and geochemical models of core formation. In: Deep Earth: Physics and Chemistry of the Lower Mantle and Core. In: AGU Monograph, vol. 217. John Wiley and Sons, Inc., Hoboken, NJ, pp. 181–190.

Rubie, D.C., Jacobson, S.A., Morbidelli, A., O'Brien, D.P., Young, E.D., et al., 2015. Accretion and differentiation of the terrestrial planets with implications for the compositions of early-formed Solar System bodies and accretion of water. Icarus 248, 89–108.

Siebert, J., Badro, J., Antonangeli, D., Ryerson, F.J., 2012. Metal-silicate partitioning of Ni and Co in a deep magma ocean. Earth Planet. Sci. Lett. 321–322, 189–197.

Solomatov, V.S., 2015. Magma oceans and primordial mantle differentiation. In: Schubert, G. (Ed.), Treatise on Geophysics, second edition, vol. 9. Elsevier, Oxford, pp. 81–104.

Stevenson, D.J., 1990. Fluid dynamics of core formation. In: Newsom, H., Jones, J.H. (Eds.), The Origin of the Earth. Oxford Press, London, pp. 231–249.

Tychoniec, L., Tobin, J.J., Agata, K., Chandler, C., et al., 2018. The VLA Nascent Disk and Multiplicity Survey of Perseus protostars (VANDAM). IV. Free-free emission from protostars: links to infrared properties, outflow tracers, and protostellar disk masses. Astrophys. J. Suppl. Ser. 288 (2), 19 pp.

Villeneuve, J., Chaussidon, M., Libourel, G., 2009. Homogeneous distribution of ^{26}Al in the solar system from the Mg isotopic composition of chondrules. Science 325, 985–988.

Visscher, C., Fegley, B., 2013. Chemistry of impact-generated silicate melt-vapor debris disks. Astrophys. J. 767, L12.

Visser, R.G., Ormel, C.W., Dominik, C., Ida, S., 2020. Spinning up planetary bodies by pebble accretion. Icarus 335, 113380.

Voelkel, O., Deienno, R., Kretke, K., Klahr, H., 2012. Linking planetary embryo formation to planetesimal formation II. The effect of pebble accretion in the terrestrial planet zone. Astron. Astrophys. 645, A132.

Wacheul, J.-B., Le Bars, M., 2018. Experiments on fragmentation and thermochemical exchanges during planetary core formation. Phys. Earth Planet. Inter. 276, 134–144.

Wood, B.J., Walter, M.J., Wade, J., 2006. Accretion of the Earth and segregation of its core. Science 441, 825–833.